GeoScienceWorld
Lithosphere
Volume 2023, Article ID lithosphere_2023_278, 19 pages
https://doi.org/10.2113/2023/lithosphere_2023_278

Lithosphere

Research Article

Monitoring Technology of Surrounding Rock Deformation Based on IWFBG Sensing Principle and Its Application

Yuanguang Zhu, Sheng Wang, Bin Liu, Xuewei Liu, and Yongshui Kang

State Key Laboratory of Geomechanics and Geotechnical Engineering, Institute of Rock and Soil Mechanics, Chinese Academy of Sciences, Wuhan 430071, China

Correspondence should be addressed to Sheng Wang; 202082010032@sdust.edu.cn

Received 13 September 2023; Published 15 December 2023

Academic Editor: Chen Guo

To address the challenge of achieving precise real-time monitoring of significant deformation in deep roadway surrounding rock, a quasi-distributed strain-sensing cable (SSC), which has a spatial resolution of 1 m, was developed based on the principle of Identical Weak Fiber Bragg Gratings. The performance of SSC has been evaluated through a series of calibration tests, revealing a range of 0%–3%, an accuracy level of 0.5%, a strain sensitivity measuring at 1.23 pm/με, and a temperature sensitivity recorded as 10.78 pm/°C. Furthermore, a real-time deformation monitoring system has been established to monitor rock deformation, consisting of SSC, supporting installation equipment, demodulation equipment, and monitoring software. Moreover, the proposed methodology was applied in the deep roadway of Guqiao coal mine. The results showed that the maximum surface displacement of the roadway is 103.47 mm, while the lateral contrast error stands at 5%. The maximum strain value of the surrounding rock measures 27,095 με. The depth of rock rupture zone is about 3 m, while the boundary of rock damage zone extends up to 6 m. This information serves as the foundation for determining the parameters of the roadway reinforcement support design.

1. Introduction

The shallow coal reserves in central and eastern China have gradually been steadily depleted due to many years of intensive mining activities. As a result, deep mining has become the predominant method for coal extraction [1, 2]. However, the excavation of deep roadways often leads to significant deformation-related disasters, such as roof collapses, extensive cracking, and floor heaving. These issues arise from the inherent conflict between the high ground stress and the low rock strength in the region [3]. Importantly, these deformations have serious implications for mine ventilation, pedestrian transportation, and the implementation of intelligent mining practices [4, 5]. According to statistics, China's deep coal mines experience hundreds of kilometers of substantial roadway deformation each year, resulting in economic losses amounting to tens of billions of yuan [6].

Monitoring both the surface and internal deformation of the surrounding rock in deep roadways over an extended period is essential to assess its stability and make well-informed decisions, such as implementing reinforcement support and performing roadway maintenance [7]. Currently, various methods are used to monitor the surface displacement of roadways, including the converging ruler method [8, 9], the electronic total station method [10, 11], the machine vision method [12, 13], and the three-dimensional laser scanning method [14]. However, relying solely on surface displacement data is inadequate for comprehensively understanding the evolution of surrounding rock stability and the extent of fracture zones, primarily due to the discontinuous nature of deep surrounding rock deformation [15]. To address this limitation, the commonly employed approach for monitoring the internal deformation characteristics of the surrounding rock is the multi-point displacement meter method [16, 17]. Nevertheless, this method has constraints related to the number of

measurement points [18], typically allowing for only five points within a 20 m drilling, resulting in limited detail in monitoring surrounding rock deformation. Additionally, indirect assessment methods like the acoustic emission method [19, 20], seismic wave method [21], and geological radar method [22] are extensively utilized to evaluate structural changes in surrounding rock. However, their effectiveness is significantly influenced by geological conditions, and they lack continuous monitoring capabilities over time. This lack of detailed data makes it challenging to provide precise information for designing roadway support parameters and determining support timing. Therefore, there is an urgent need to develop advanced monitoring technology for measuring surrounding rock deformation in deep roadways.

Optical fiber sensing technology is widely employed in various engineering fields, including mining, water conservancy, hydropower, and civil transportation, owing to its high precision, intrinsic insulation, and resistance to electromagnetic interference [23–25]. Fiber optic sensing technology accomplishes the measurement of physical quantities by detecting changes in light wave characteristic parameters, such as wavelength, phase, light intensity, and polarization state, induced by external factors like temperature, stress, vibration, and magnetic fields [26–28]. Zhao et al. [29] introduced a method for delineating coal mine roadways based on Fiber Bragg Grating (FBG) sensing technology, which monitors layer displacement. This method offers the advantages of high sensitivity and robust antiinterference measures [30]. However, it is worth noting that most commercial FBG demodulators have a limited demodulation range, which constrains the number of sensing points and their density within the optical fiber [31]. Bin Tang [32] developed an innovative, fully distributed sensing and monitoring system for perimeter rock deformation based on Brillouin Optical Time-Domain Reflectometry technology. This method requires only a single optical fiber to conduct distributed strain and temperature measurements across all defined areas, activated by laser pulses. As a result, it can replace numerous discrete sensors [33, 34]. Nevertheless, it falls short in terms of resolution and measurement accuracy. Binyang Sun [35] utilized Brillouin Optical Time-Domain Amplification sensing cables to continuously monitor the internal deformation of the enclosing rock in roadways. This approach facilitated the identification of the mechanisms underlying rock deformation damage. The method excels in terms of its resolution and ability to measure fine details, making it particularly well-suited for small-scale deformation measurements in laboratory settings. However, its widespread application in the field is constrained by the high cost of demodulation equipment. In a different approach, Zhang Manliang et al. [36] introduced a quasi-distributed fiber-optic sensing scheme based on Identical Weak Fiber Bragg Gratings (IWFBG), leveraging the low reflectivity of ultra-weak reflective gratings. Li Bo [37] and Wang Yiming [38] investigated the demodulation method for quasi-distributed fiber with IWFBG. This method is distinguished by its high capacity, exceptional accuracy, and remarkable density. Furthermore, its cost-effective signal demodulation facilitates its use in engineering applications. The principal challenge in deploying fiber optic sensing technology in practical field applications lies in the complexity of monitoring significant deformations in the surrounding rock, primarily attributable to inherent material ductility flaws.

To address the issues previously mentioned, this study has developed a quasi-distributed, large-range strain-sensing cable (SSC) designed for monitoring the deformation of roadway rock. This cable incorporates large-strain fiber optics and is based on the IWFBG principle. A real-time deformation monitoring system (RTDMS) has been developed using the SSC, enabling remote and precise monitoring of the deformation in deep roadway rock. The cable and system's performance parameters and reliability were rigorously assessed through both laboratory calibration tests and field industrial tests. This study introduces a novel method for monitoring the deformation of rock in the vicinity of deep roadways. This innovative approach provides scientific guidance and invaluable data to support decision-making in the management of rock stability.

1.1. SSC Development Based on IWFBG

1.1.1. Principle of IWFBG Strain Sensor. Optical fiber sensors leverage the light-sensitive properties of fibers to create a spatial phase grating within the fiber core. This grating serves as a reflective structure within the fiber core, altering the effective refractive index either periodically or nonperiodically [39]. In contrast to traditional Bragg gratings, ultra-weak reflective FBGs [40] typically exhibit reflectivities below −20 dB [41], with peak reflectivities below 1% [42]. The lower reflectivity enhances the transmission of light waves through the grating, thus increasing the sensing network's capacity.

In a fiber grating sensing network, there is a difference in the timing of wavelength signals reflected back from any two sensors connected in series on the same transmission fiber. Optical time-domain reflectometry technology [43] utilizes the time-domain characteristics of the fiber grating to identify the sensor's location by measuring the signal's return time to the terminal. The spectral information of any fiber grating can be accurately determined through appropriate calculations. Optical time-domain reflection technology eliminates the bandwidth constraints associated with the system's light source and minimizes external environmental limitations on the fiber optic sensing network as a whole. Moreover, this technology significantly augments the capacity of the sensing network.

Figure 1 shows the principle of IWFBG sensor. Pulsed light is emitted from a light source into the fiber core through the coupler. The light wave with the same wavelength as the incident light (P_{in}) is reflected at the grating, while most of the transmitted light (P_t) continues to propagate forward. The reflected light (P_r) from the core can be demodulated by the demodulation system at different time intervals. As the fiber core experiences simultaneous deformation, often caused by the surrounding

rock deformation, the refractive index of the Bragg grating changes. This alteration in the refractive index subsequently modifies the central wavelength of the reflected light. The magnitude of the strain is indicated by the change in the central wavelength of Pr ($\Delta\lambda$). The sensing network is made up of low-reflectivity gratings which make its transmission characteristics comparable to a distributed fiber optic sensing network. However, it is important to note that the fiber grating sensing network exhibits higher reflectivity compared with the distributed sensing network, resulting in significantly enhanced sensing accuracy [44].

According to the theory of fiber coupling [45], changes to the Bragg grating cause alterations in its grating period and refractive index, resulting in a displacement of the central wavelength of the reflected light wave [46, 47].

$$\frac{\Delta\lambda_b}{\lambda_b} = \frac{\Delta\Lambda}{\Lambda} + \frac{\Delta n_{eff}}{n_{eff}} \tag{1}$$

where λ_b is the central wavelength, n_{eff} is the refractive index of the core, and Λ is the grating period.

Changes in the refractive index of the fiber core are primarily caused by external forces and temperature in the field application environment. When deformation occurs due to external forces causing a change in the refractive index of the fiber core, Equation (1) can be expressed as follows:

$$\frac{\Delta\lambda_b}{\lambda_b} = \left(1 + P_e\right)\varepsilon \tag{2}$$

where ε is the fiber strain value; P_e is the effective photoelasticity coefficient of the fiber, $P_e = \frac{1}{2}n^2\left[\left(1-\mu\right)P_{12} - \mu P_{11}\right]$; P_{11} and P_{12} refer to the elasticity coefficients of the fiber, which are the change coefficients of the longitudinal and transverse refractive indices of the grating; and μ is the Poisson's ratio.

Defining $K_T = (\alpha + \xi)\lambda_b$ as the sensor strain sensitivity coefficient, then there is:

$$\Delta\lambda_b = K_\varepsilon\varepsilon \tag{3}$$

When considering only the temperature as the influencing factor on the grating central wavelength, Equation (1) can be expressed as:

$$\frac{\Delta\lambda_b}{\lambda_b} = (\alpha + \xi)\Delta T \tag{4}$$

where α is the thermal expansion coefficient of the fiber material and ξ is the thermo-optical coefficient of the fiber material, which indicates the relationship between the refractive index of the fiber and temperature changes.

Defining $K_T = (\alpha + \xi)\lambda_b$ as the sensor temperature sensitivity coefficient, we have:

$$\Delta\lambda_b = K_T\Delta T \tag{5}$$

Equation (3) and Equation (5) show the relationship between wavelength change and strain and temperature. However, it is essential to acknowledge that variations in fiber grating materials, differences in grating fabrication techniques, and the impact of environmental factors during the packaging of fiber optic sensors can lead to variations in the strain sensitivity coefficient among different fiber gratings. Consequently, upon the completion of the internal packaging of the fiber grating sensor, it becomes necessary to conduct indoor sensor testing. This is a critical step in the calibration of FBG sensors, aimed at determining the values of K_ε and K_T.

1.1.2. Development of SSC. Fiber grating sensing technology is commonly employed in various fields due to its high resistance to interference and accurate measurements. However, the limitations of the core fiber material render it unable to withstand substantial strains, thereby constraining the application of fiber optics in monitoring significant deformations. In this study, the utilization of ultra-weak reflective fiber with high-strain tolerance enables the deployment of fiber grating sensors for monitoring the deformation of rock surrounding roadways. On this basis, a quasi-distributed SSC has been developed based on the principle of IWFBG. On the basis of giving full play to the high sensitivity and strong antiinterference of fiber-optic technology, it increases the capacity of the sensing network and reduces the cost of demodulation.

Figure 2 shows a structure and physical diagram of the SSC. The SSC comprises a fiber core, a metal spiral armor, steel strands, and a polyethylene sheath from the inside to the outside. The core is etched with ultra-weak reflectivity FBG [48], and the outer structure is mainly to protect the core. In the process of SSC, a metal spiral armor and steel-stranded wire are passed through a stranded bite. Subsequently, the outer jacket layer is then extruded at high temperature onto the steel-stranded wire. The binder is used to fill the gap between the metal spiral armor and the bare fiber, ensuring proper curing into the anchor point. These structures protect the fiber core while also ensuring the outer sheath, stranded wire, metal spiral armor, and fiber optic core work together to resist deformation. By charging the adhesive into the gap between the metal spinning armour and the optical fibre, the adhesive solidifies and hardens into a bonding anchor point. This treatment ensures that the outer external structures and the fiber core will undergo synergistic deformation under the action of external forces. The anchor design spacing is 1 m, and the outer diameter of the cable is 6 mm. The FBG design is positioned between two anchor points. The length of the grating area is less than 10 mm, with a single wavelength center at 1530 nm. The reflectivity of the fiber grating is 0.05%.

1.2. Performance Test of SSC. In order to understand the measurement characteristics and error indicators of the SSC, the performance of the cable is tested based on "JJF

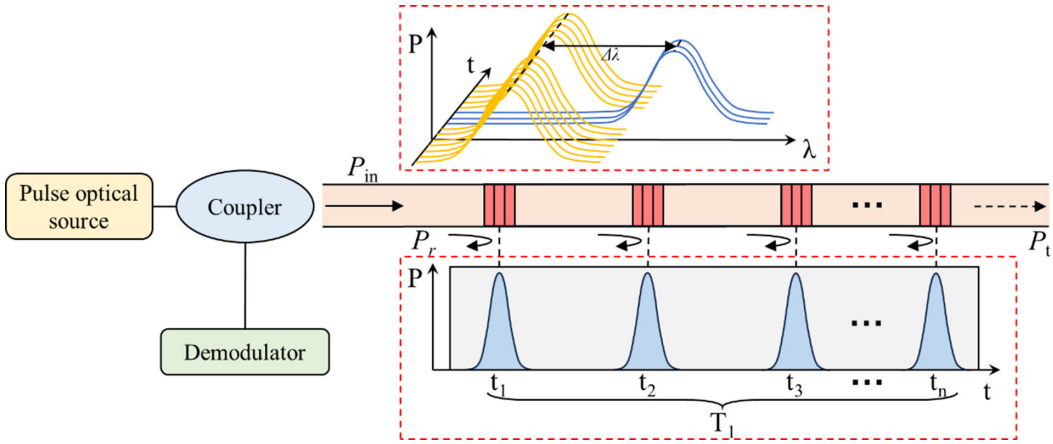

Figure 1: Principle diagram of IWFBG sensors.

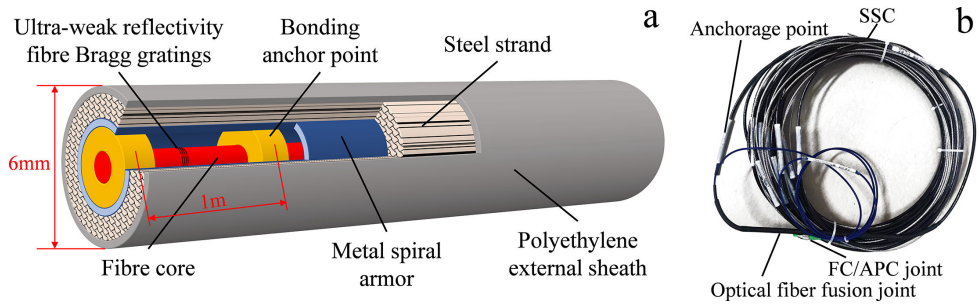

Figure 2: Principle diagram of IWFBG sensor. (a) Structure diagram. (b) Physical diagram.

1305–2011 Calibration Specification for Line Displacement Sensors" and "JG/*T* 422–2013 Fiber Optic Grating Strain Sensors for Civil Engineering" as references.

1.2.1. Strain Calibration. IWFBG sensor can accept more grating reflection spectra than a normal fiber grating due to its lower reflectance. This allows for a larger strain measurement capacity. To assess the strain range of the SSCs, a displacement tensile platform is employed to perform a comprehensive set of strain tensile measurements. Meanwhile, to successfully demodulate the wavelength data generated by the large-range strain stretching, the data acquisition equipment utilizes a high-capacity ultra-weak grating analyzer, as depicted in Figure 3. The device can accept the central wavelength of the reflectance spectrum range at 1528–1568 nm.

During the stretching of the fiber grating, it is crucial to ensure that the displacement of the central wavelength falls within the equipment's wavelength acceptance range or closely approaches its boundaries. This precaution guarantees the clear visibility of the central wave peak. The acquisition of data regarding the central wavelength of the grating is typically linear; there exists a predictable relationship between strain and the degree of wavelength change. When stretching the fiber grating, the displacement of the central wavelength should be within the wavelength acceptance range of the equipment or close to the boundary of the equipment acceptance. This will ensure that the center of the wave peak is clearly visible. Grating central wavelength data acquisition is normal; there is a linear relationship between strain and the amount of wavelength change. However, when the displacement of the central wavelength exceeds the monitoring boundary of the equipment, the collected data tend to exhibit irregular fluctuations, making normal data collection impossible.

Figure 4 shows the strain calibration procedure of SSC. The process of strain calibration begins by ensuring that the fiber grating is uniformly subjected to axial strain, accurately representing the strain across the entire length of the fiber. The length of the SSC fixed between the two fixtures is 1 m, and the displacement of the tensile platform has an accuracy of 0.01 mm. When the tensile platform moves 10 mm, the SSC generates a strain value of 1%. The specific calibration procedures are as follows: (1) Securely affix both ends of the SSC to the fixed end and the fixed base. (2) Incrementally move the displacement platform from its initial position in 2 mm intervals. Simultaneously, record the central wavelength of the FBG at the calibration terminal. (3) Upon reaching a stretching distance of 30 mm, move the fixed base in the opposite direction while continuing to record the central wavelength of the FBG at 2 mm intervals. The experiments are designed to encompass a range of stretching from 0 to 30 mm, with three sets of cyclic stretching conducted for accuracy and reliability.

The test data have been analyzed and fitted with a linear equation, resulting in the strain calibration test strain-wavelength curve presented in Figure 5. The fitted curve equation is $y = 12.30x + 1530.287$. Based on this

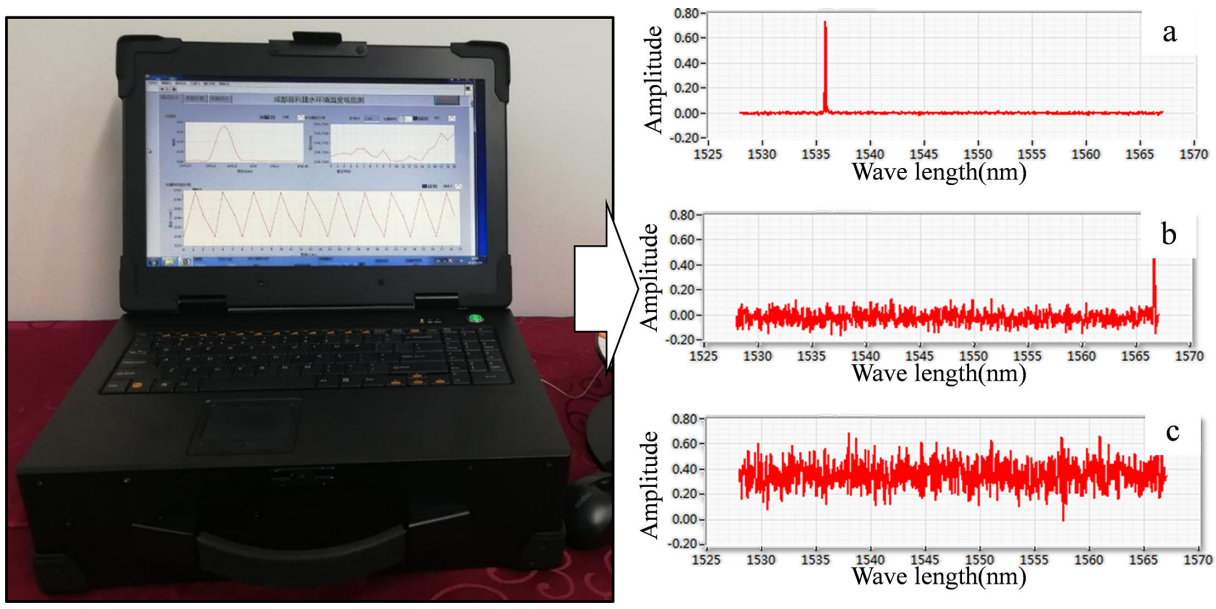

Figure 3: High-capacity ultra-weak grating analyzer. (a) The grating array wavelength diagram in the wavelength range. (b) The wavelength diagram of the boundary grating array in the wavelength range. (c) The wavelength diagram of the grating array outside the wavelength range.

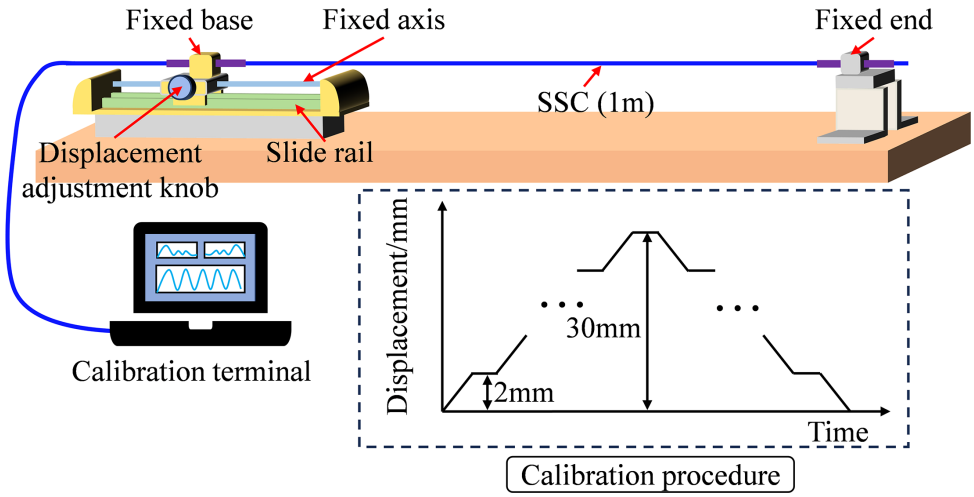

Figure 4: Strain calibration procedure of SSC.

equation, the strain sensitivity coefficient of the SSC can be determined as 1.23 pm/με. Table 1 provides information on various calibration parameters of the SSC as follows:

(1) Full-scale output value: This parameter represents the algebraic difference between the upper limit and the lower limit of the output value within the measuring range of the SSC.

(2) Strain sensitivity: It measures the extent of wavelength change in the SSC when subjected to an external load. This parameter quantifies the device's responsiveness to changes in strain.

Table 1: Calibration parameters of SSC.

Properties	Index	Numerical value
Sensing characteristic	Maximum strain value (%)	3.00
	Full-range output value Y_{FS} (nm)	36.93
	Strain sensitivity K_T (pm/με)	1.23
Measurement error (Accuracy level)	Basic error δ	0.47% (0.5)
	Return error h	0.35% (0.5)
	Linearity l	0.07% (0.5)
	Reproducibility r	0.23% (0.5)

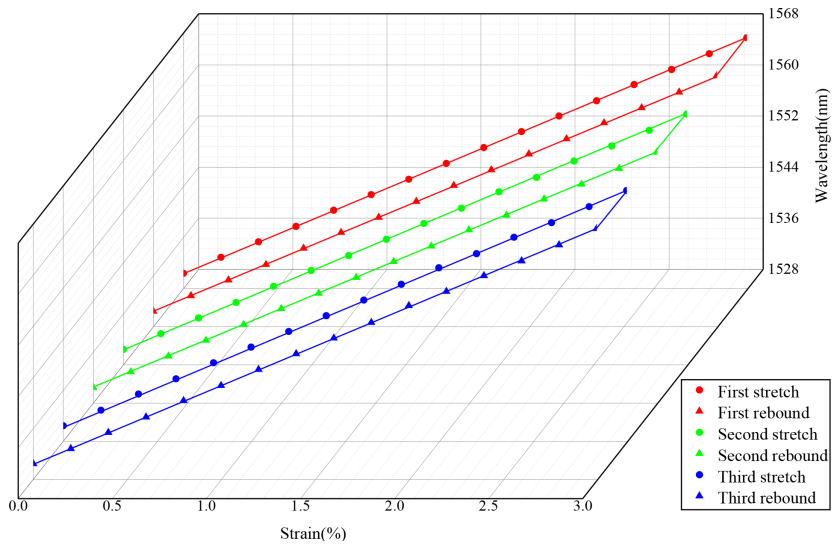

Figure 5: Strain-wavelength curve of SSC.

(3) Basic error: The basic error is an indicator that contributes to stabilizing the measurement accuracy of the entire instrument. It reflects the inherent accuracy and precision of the SSC in its measurements.

(4) Return error: This parameter is the absolute value of the difference between the measured value and the actual value when the SSC is loaded in different directions under the same conditions. It accounts for any discrepancies in measurement accuracy when the load direction changes.

(5) Linearity: Linearity is expressed as the absolute value of the difference between the measured value and the value predicted by the fitted curve equation ($y = 12.30x + 1530.287$). It serves as a measure of how closely the actual measurement data align with the predictions made by the linear model, assessing the accuracy of the calibration.

(6) Repeatability: Repeatability refers to the consistency of the calibrated instrument's output data at each calibration point. It assesses how reliably the SSC provides consistent measurements when exposed to the same conditions or loads on multiple occasions.

1.2.2. Temperature Calibration. The temperature calibration test for the SSC is a crucial step to account for the sensor's sensitivity to changes in ambient temperature, which can interfere with accurate strain measurements in real engineering applications.

The process of temperature calibration testing is shown in Figure 6:

(1) Preparation: To ensure that the strain measurements are not affected by SSC sliding or other external factors, the SSC is fixed in place and positioned inside a temperature-regulating chamber.

(2) Data Collection Setup: One end of the SSC is threaded through the temperature-regulated chamber, and it is connected to a calibration terminal. This setup allows the collection of test data while maintaining a stable configuration.

(3) Temperature Points: The temperature calibration experiment involves setting up nine temperature points. It starts at 10°C and proceeds in 10°C intervals. Each temperature point is allowed to stabilize for approximately 60 minutes.

(4) Data Recording: During the stabilization period at each temperature point, the wavelength values are recorded for the corresponding temperature.

The measured test data were analyzed and linearly fitted to obtain the temperature calibration test temperature-wavelength curve shown in Figure 7. The fitted curve equation is $y = 10.78x + 1530.3112$, and the measured temperature sensitivity coefficient of the SSC is 10.78 pm/℃. According to the correlation coefficient test method, the square of the correlation coefficient of the linear regression equation is calculated to be 0.999. This indicates a strong linear relationship between the change in SSC central wavelength and the change in ambient temperature. By taking into account the specific value of the ambient temperature, the interference of the wavelength signal from the SSC field strain test can be eliminated.

1.3. RTDMS for Deep Roadway Surrounding Rock

1.3.1. System Composition. To complement the field application of the SSC, this study incorporated an embedded strain demodulator (ESD) utilizing IWFBG technology (Figure 8). A pulsed light source present within the

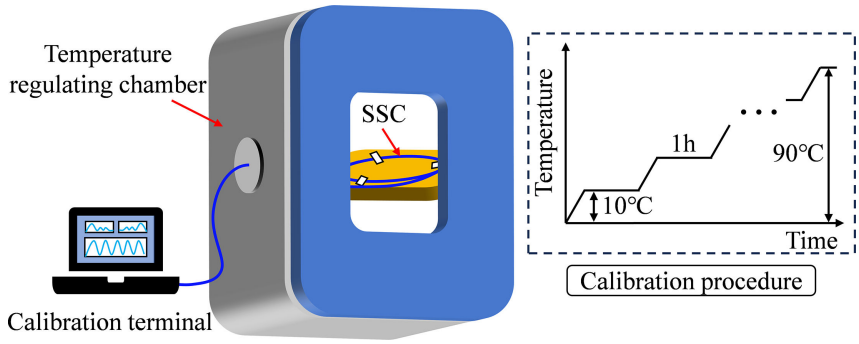

Figure 6: Temperature calibration procedure of SSC.

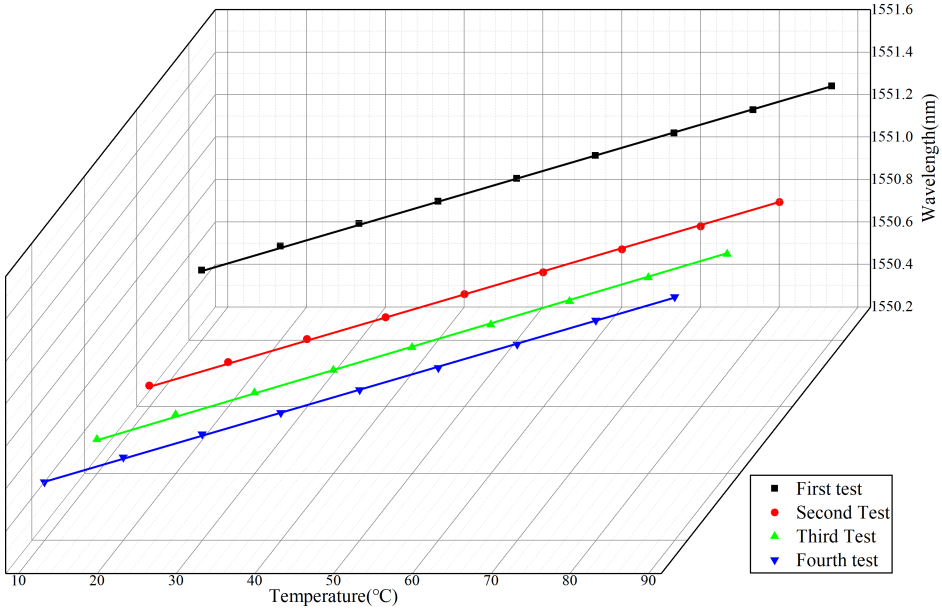

Figure 7: Temperature-wavelength curve of SSC.

ESD emits near-infrared laser pulses. As the laser pulses propagate in the forward direction along the fiber, they are reflected by an array of sensors connected in series on the fiber. This reflected light is returned back along the fiber in the dorsal direction to the acquisition card where it is detected and analyzed in real time. Equipped with built-in ARM and Linux operating systems, the ESD can run demodulation algorithms at low/high speeds to acquire the position, temperature, or strain values of each sensor and transmit them back. ESD combines high-speed acquisition and underlying demodulation with the advantages of high integration, good stability, rich software functions, and convenient secondary custom development. For specific technical details, please refer to Table 2.

In order to meet the requirements of different field monitoring works, ESD has reserved a variety of data communication interfaces. This allows for flexible networking (Figure 8). During the installation process, you can select the appropriate communication mode based on the site conditions. This allows automated remote monitoring via either a wired or wireless connection to the LAN/WAN.

Based on the SSC and ESD, a supporting monitoring software (Figure 9) has been developed. This software enables the automatic collection, storage, and processing of monitoring data. It comprises four main segments: operation status, parameter setting, test mode, and data preservation. This versatile software allows for real-time monitoring of wavelength, temperature, and stress data. Furthermore, it incorporates remote operation capabilities, enabling users to remotely monitor, control, and archive data.

Furthermore, the testing system comes with a set of installation equipment (Figure 10). The first component is a push rod, working in conjunction with oriented components to precisely position the SSC within the designated location of the test drilling. Fixed anchor is used to ensure that the SSC remains securely in place within the roadway rock. Finally, a flange serves to establish a connection between the SSC, the optical fiber jumper, and subsequently, the ESD.

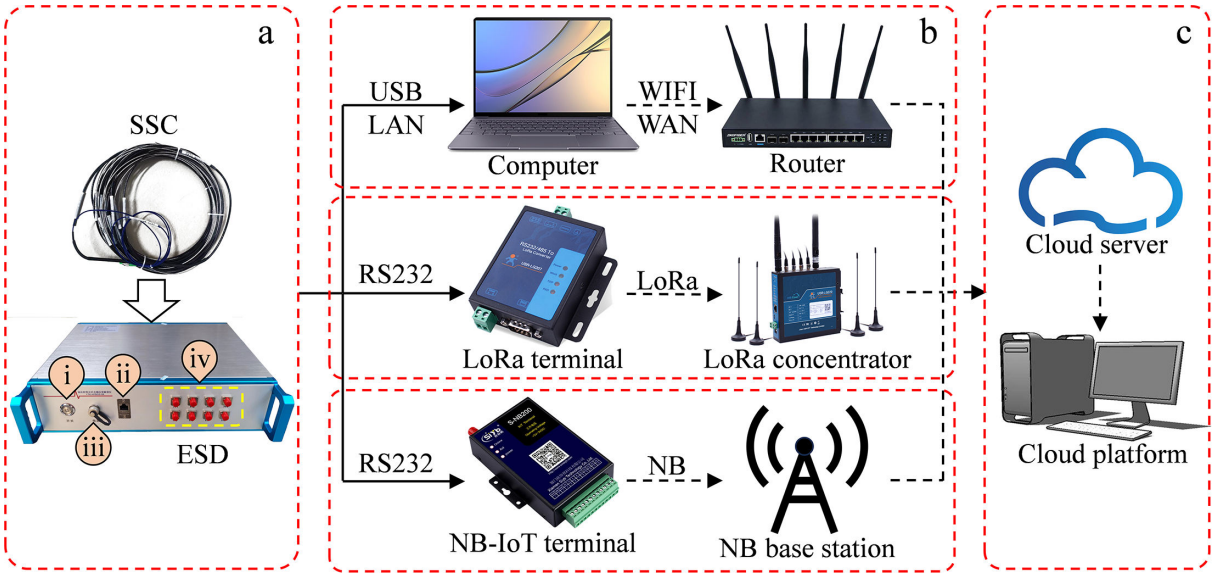

Figure 8: ESD and data transmission network diagram. (a) Front end with the power switch, power supply interface, communication interface, and demodulation channel. (b) Network mode. (c) Back end.

Table 2: Technical parameter table of ESD.

Performance index	Equipment technical parameters
Wavelength coverage	1528–1568 nm
Wavelength repeatability accuracy	±2 pm
Number field of channels	Eight channels (extensible)
Sampling rate	250 MHz
Reflectivity of FBG	0.001%–0.1%
Full-band demodulation frequency	≤1 Hz
Spatial resolution of the same wavelength	≥1 m
Single-channel measurement length	≤15 km
Number of single-channel measuring points at the same wavelength	≤5000
Data output interface	Ethernet port
Interface type	FC/APC, compatible with conventional single-mode communication fiber
Power supply and rated power consumption	12 V, 16 W
Overall dimension	360 × 375 × 100 mm
Weight	5 kg

1.3.2. Field Operation Process. The field operation process is described based on the SSC strain monitoring principle, with a detailed illustration of the specific steps shown in Figure 11.

1.3.2.1. Surrounding Rock Drilling. At the designated test site, a geological drilling rig is used to prepare the test drill drillings at the specified location. The depth of the drilling should be no less than five times the diameter of the drilling, with a minimum diameter of 70 mm. After drilling to the designated depth, the debris in the drilling should be cleared to ensure a smooth and mostly water-free drilling.

1.3.2.2. SSC Pushing. Before installing the SSC, the front end of the SSC is secured to the fixed anchor located at the front end of the first push rod. It is then slowly pushed forward by human power until it is fed into the predetermined position. The other end of the SSC connector is left open for drilling, and the push rod is withdrawn. Attention should be given to maintaining the cable in a straight configuration within the drilling by gently tensioning the cable.

1.3.2.3. Grouting and Backfilling. Following the SSC installation, grouting pumps are used to inject microexpansion fast-setting cement slurry into the test drilling. In the grouting process, bags are used to seal the drilling and prevent the slurry from flowing out of the pipe after the grouting is completed. It is important to fill the entire drilling densely in order to ensure full contact between the SSC and the rock mass surrounding the drilling and to achieve a synergistic deformation with the surrounding rock. The fixed anchor ensures that the SSC remains straight and in the same position during grouting and slurry consolidation.

1.3.2.4. Strain Data Testing. Once the hole has been grouted, the SSC connector left in the drilling is connected to the ESD using optical fiber jumper and flanges. And through the data transmission line, the ESD and the test terminal will establish a connection to carry out field signal testing and verify the transmission of equipment signals.

After the installation of the SSC, it was flanged to optical fiber jumpers to establish the final link to the ESD. Afterward, it is linked downhole to an Ethernet switch using

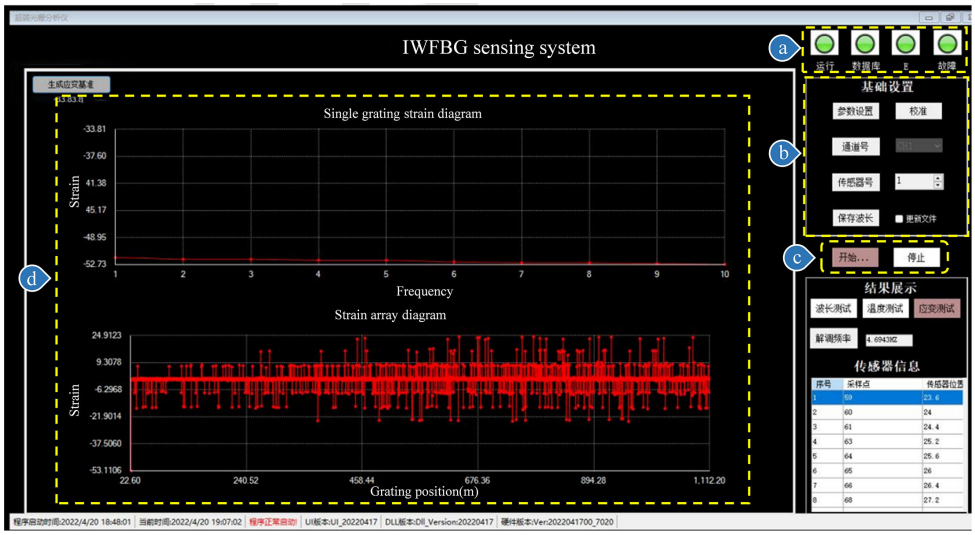

Figure 9: Monitoring software. (a) The running state of the test system. (b) The basic setting option. (c) The monitoring control button. (d) The area where the monitoring results are presented.

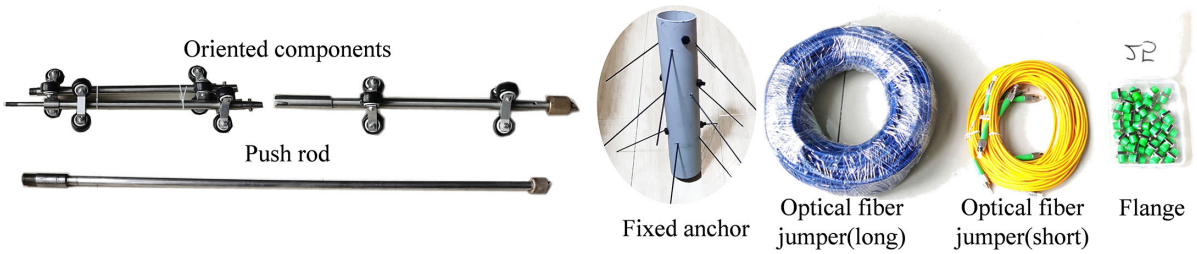

Figure 10: Installation equipment.

a data cable. In mines with high levels of gas; ESD and Ethernet switches should be stored together in an explosion-proof box that has been customized for this purpose. Monitoring data are sent to the terrestrial terminal via underground data transmission. With supporting monitoring software, RTDMS achieves remote control, real-time monitoring, and data storage of underground monitoring system. Wavelength data collection began immediately after the slurry solidified in the test drilling. The change in wavelength data measured over time during the test period is used to calculate the strain values in the surrounding rock. Based on this, we analyze the long-term evolution law of internal deformation of the surrounding rock and obtain the migration deformation data of the surrounding rock in the deep roadway. The SSC, in conjunction with the supporting installation equipment, demodulation equipment, and monitoring software, constitutes the RTDMS for deep roadway (Figure 12).

2. Engineering Application

2.1. Engineering Background. The Guqiao Mine is located in the northwest of Fengtai County, Anhui Province, covering an area of approximately 140 km^2. The monitoring sites for RTDMS are located in the rail transport roadway (II) and belt conveyor roadway. The depth of both roadways is 823 m, and the surrounding rocks are mainly composed of sandy mudstone. The rail transport roadway serves as the primary coal outlet channel in the southern area. In order to avoid the influence of the fault crushing zone, a "V" shaped diversion is used in the construction process. This detour design inadvertently introduced redundancy in the main coal discharge system, leading to a reduction in coal discharge efficiency. The roadway support adopts anchor net spraying to ensure stability and prevent significant deformation of the roadway. The belt conveyor roadway, on the other hand, traverses a fault zone with fractured surrounding rock, making the construction conditions notably intricate. To address these challenges, the roadway support system adopts a U-shaped shed along with anchor net spraying support. Importantly, no repairs have been carried out on the roadway since its initial construction and usage. Consequently, the roadway has experienced varying degrees of deformation at present.

Due to the complex geological conditions of the deep coal mine roadway, the on-site roadway deformation monitoring system cannot achieve comprehensive distributed monitoring of the entire roadway. Therefore, it is necessary to select a reasonable and representative monitoring section that can effectively improve the accuracy of the perimeter rock monitoring results. This will allow the monitoring data to truly reflect the deformation of the perimeter rock of the deep roadway. At the same

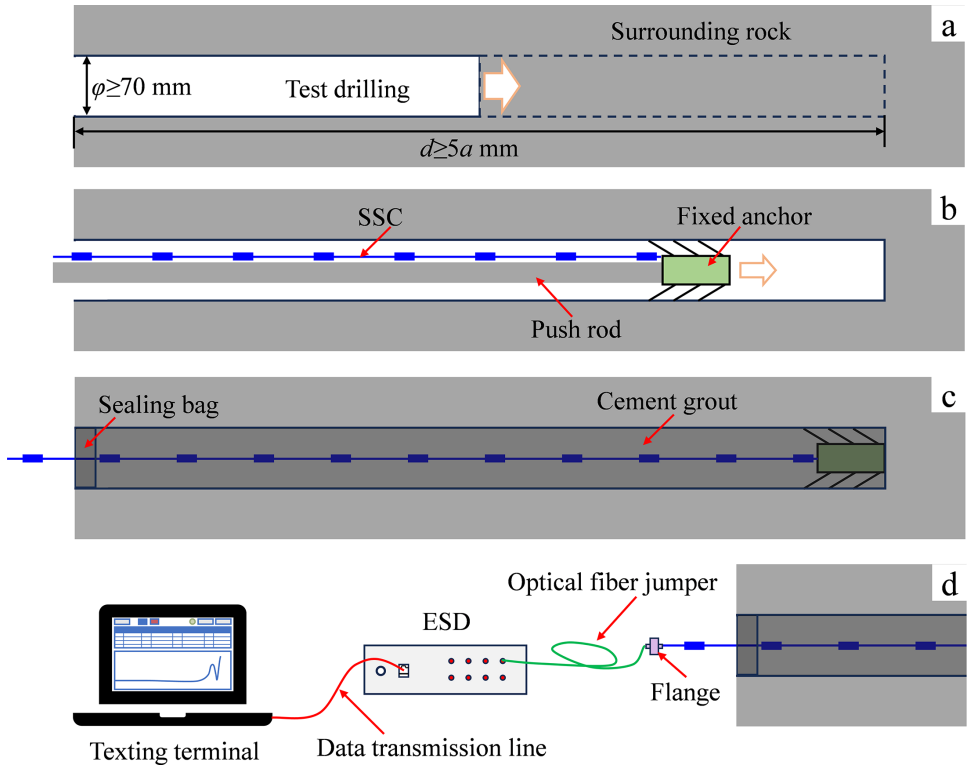

Figure 11: Field operation process of SSC. (a) Surrounding rock drilling where φ is the drilling diameter, d is the drilling depth, and a is the roadway diameter. (b) Strain-sensing cable pushing. (c) Grouting and backfilling. (d) Strain data testing.

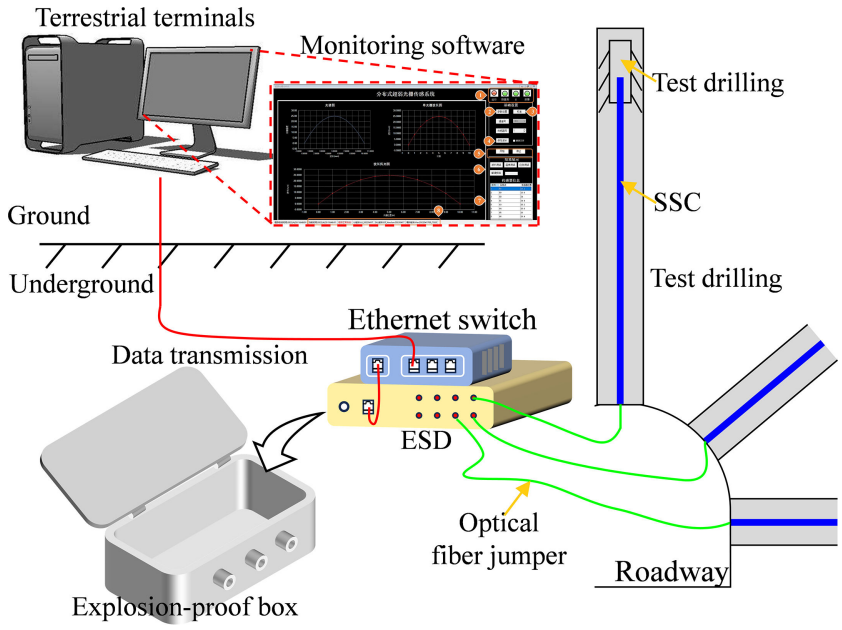

Figure 12: Field operation process of SSC.

time, the selection of test locations should also consider the convenience of connecting the perimeter rock deformation monitoring system, minimizing the use of fiber optic connectors, and avoiding energy loss. According to the aforementioned requirements for selecting test locations, two locations have been chosen for the implementation of roadway surrounding rock deformation monitoring. The specific locations can be seen in Figure 13.

Monitoring Section 1 is strategically positioned at the intersection of the rail transport roadway (II) and the "V" bypass fault. This area is particularly susceptible to roadway rock instability compared with other locations. Establishing

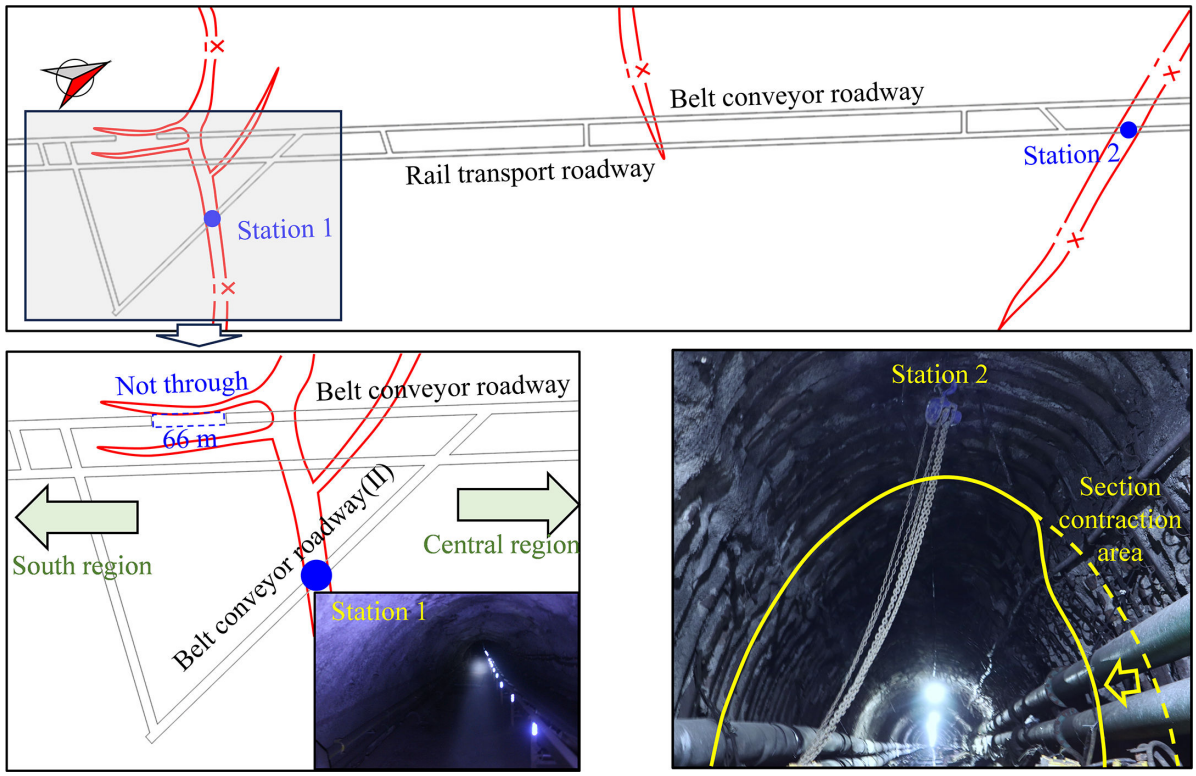

Figure 13: Monitoring roadway location map.

a monitoring section here allows for real-time observation of the movement and deformation of the rock surrounding the roadway. The data collected in this section provide essential support for the stabilization efforts in the rail transport roadway.

Monitoring Section 2, located at the intersection of the belt conveyor roadway, is crucial due to significant deformations observed on the right side of the roadway, as indicated in Figure 13. To ensure the normal use of the roadway, repairs are necessary to rectify the substantial deformation. By implementing a monitoring section in this area, the real-time deformation of the surrounding rock can be closely monitored. This continuous monitoring enables accurate assessments of the stability of the surrounding rock, offering valuable guidance for subsequent repair and support work on the heavily deformed roadway.

2.2. Monitoring Propose. In order to comprehensively understand the deformation of the surrounding rock in the section, test drillings were placed at the gang (0°), top (90°), and shoulder (145°) of the roadway to monitor the deformation of the surrounding rock structure. Three SSCs were installed in each section and labeled A to E. The test drillings had a maximum depth of approximately 20 m and a diameter of 73 mm (Figure 14). In order to prevent additional damage to the surrounding rock caused by drilling, which could result in further destabilization of the zone, no measurement points were placed in the region where significant deformation of the roadway's surrounding rock occurred.

The field test procedure is shown in Figure 14, and the specific operational procedure is as follows: (1) Before installing the equipment, check the SSC to ensure its integrity and verify that the equipment connection is intact and the signal transmission is normal. (2) According to the test program (Figure 15), open a drilling in the corresponding position of the roadway. (3) Secure the SSC with the push rod and insert it into the designated position of the test drilling. (4) Seal and grout the test drilling until the slurry flows back. (5) Use portable fiber optic demodulation test equipment to verify the normality of signal transmission after the installation is completed.

Following the successful installation and commissioning of the rock engineering deformation monitoring system (REDMS), the monitoring of surrounding rock deformation in the deep roadway commenced. The total duration of testing extended for 90 days, with data collection taking place every 3 hours. The REDMS consistently collected wavelength and strain data from the surrounding rock, which were then regularly exported, organized, and analyzed. This analysis was instrumental in assessing the movement and deformation of the roadway's surrounding rock over time.

2.3. Monitoring Results and Analysis. Based on the wavelength signal variation obtained by ESD and the calibration coefficients of the SSC, the strain curves of each test drilling of the roadway surrounding rock in each monitoring section were calculated (Figure 16 and Figure 17). The strain generated by the tensile deformation of the surrounding rock was set as positive, while the strain

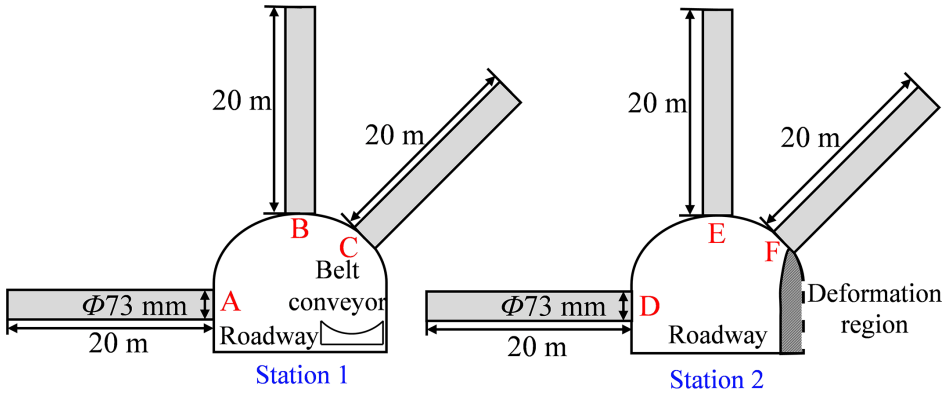

Figure 14: Schematic layout of monitoring section (1 and 2) drillings.

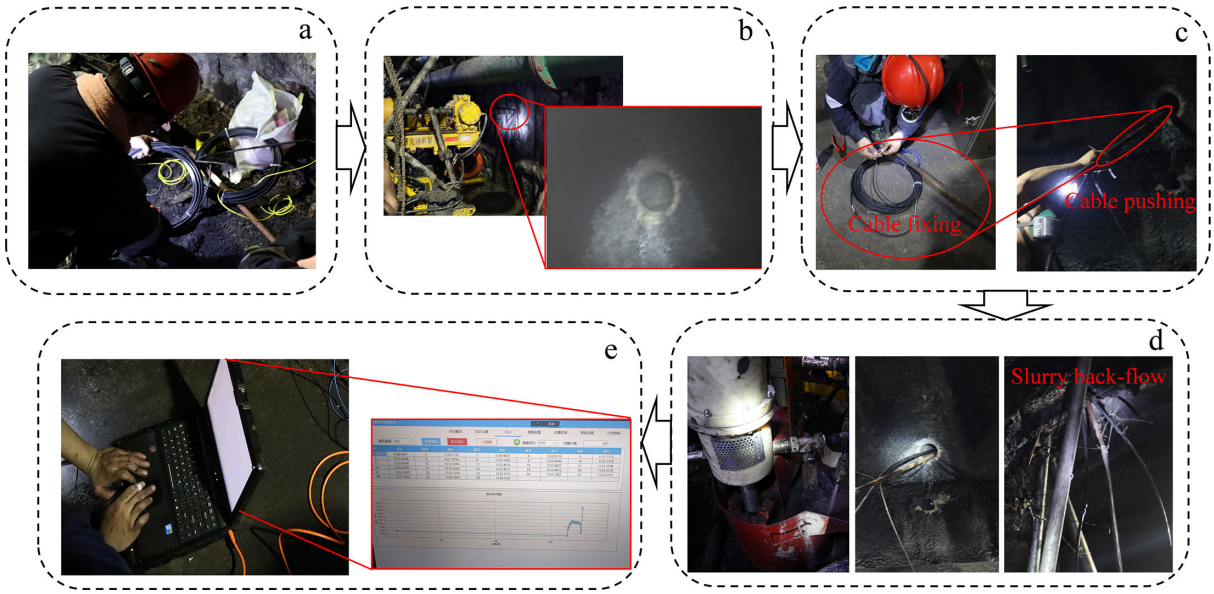

Figure 15: Field test procedure. (a) Inspection before installation. (b) Drilling in surrounding rock. (c) Installation of strain sensing cable. (d) Backfill grouting. (e) Strain data monitoring.

generated by the compressive deformation of the surrounding rock was set as negative. As there is almost no deformation of the surrounding rock beyond the 10 m range, only the strain of the surrounding rock within 10 m is considered.

Figure 16 shows the time sequence curve for strain monitoring of the surrounding rock in each test drilling of the roadway in monitoring section 1. Notably, among all the test drillings, test drilling A exhibits the most significant deformation. The most prominent strain occurred in the range of 3–4 m, registering at only 84 με. This deformation is primarily characterized by tensile strain, indicating a gradual increase in tensile deformation within the surrounding rock over time. Conversely, the strain monitoring data of drilling B are within the range of −8–12 με, which is caused by the measurement error of the SSC and the vibrations of the surrounding rock of the roadway itself. The strain value fluctuates around zero, with no obvious upward trend. This indicates that the surrounding rock of the roadway is stable, and no deformation is detected. The strain monitoring data of drilling C varied from −26 to 29 με. During the monitoring period, the surrounding rock at drilling C exhibited noticeable compression deformation at depths of 0–2 m and 3–4 m. This is due to the expansion of the surrounding rock damage in the range of 2–3 m and >4 m squeezing of the surrounding rock on both sides. Compared with the deep surrounding rock, the shallow surrounding rock is more susceptible to vibrations from the roadway surface. The strain curve indicates that the shallow surrounding rock experiences greater fluctuations in strain compared with the deep layer. The deformation of the surrounding rocks in monitoring section 1 is small and can be classified as elastic deformation. It shows that the support structure here is intact, and the surrounding rock is stable. Therefore, we do not analyze the absolute displacement or the range of the rupture zone of the surrounding rock here.

Figure 17 shows the time sequence curve for strain monitoring of the surrounding rock for each test drilling of the roadway in monitoring section 2. Among them, the

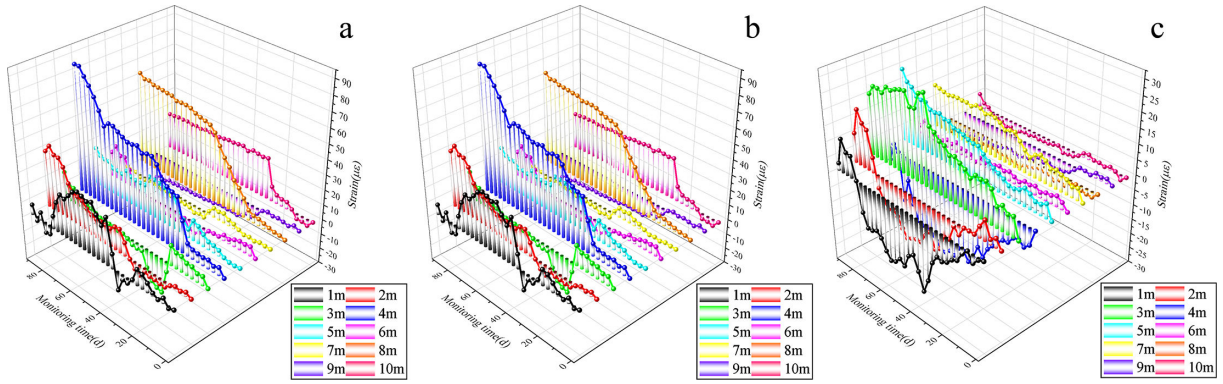

Figure 16: Monitoring section 1 roadway surrounding rock strain time series diagram. (a) Drilling A. (b) Drilling B. (c) Drilling C.

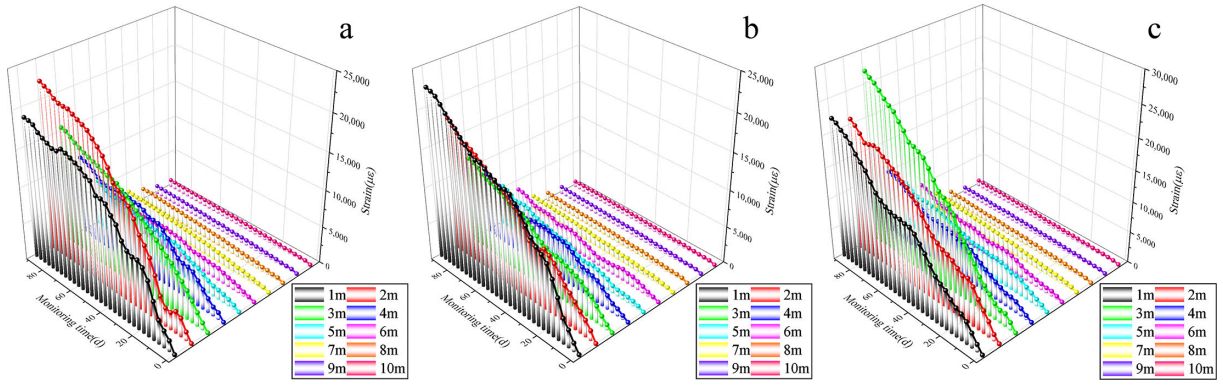

Figure 17: Monitoring section 2 roadway surrounding rock strain time series diagram. (a) Drilling D. (b) Drilling E. (c) Drilling F.

maximum deformation of drilling D occurred at 1–2 m of surrounding rock (22,394 με). The maximum deformation of drilling E occurred at 0–1 m of surrounding rock (22,526 με). The maximum deformation of drilling *F* occurred at 2–3 m of surrounding rock (27,095 με). All curves indicate that the tensile deformation of the surrounding rock increases over time, resulting in a larger strain being generated. This indicates that the surrounding rock at monitoring section 2 has not yet reached a stable state and is still undergoing continuous deformation. The maximum strain of the surrounding rock varies between different drillings, and the deformation of the surrounding rock within the same drilling fluctuates. Such discrepancies can be attributed to the fact that the deformation and rupture patterns of the surrounding rock in the roadway display marked discontinuities in both temporal and spatial dimensions.

Figure 18 shows the distribution curve of the absolute displacement of the surrounding rock in monitoring section 2 at 90 days. Notably, all measurements were taken at depths exceeding 20 m, more than five times the radius of the roadway. It can be considered that the deepest point in the drilling remains stationary, serving as the reference point. Using the deepest point as the base point, the displacement of any other point relative to the deepest point is the absolute displacement of that point [49]. The data reveal a gradual decrease in absolute displacements in the surrounding rock as depth increases. Deformation in the roadway's surrounding rock primarily occurs within a 10 m range, with the maximum absolute displacement observed at the surface of the roadway. In detail, the absolute displacement of the surrounding rock at drilling D is 85.67 mm, with 80.01% of the deformation occurring within a 4 m radius of the drilling. The absolute displacement of the surrounding rock at drilling E is 76.45 mm, with 79.92% of the deformation is generated within 4 m in the surrounding rock. The maximum absolute displacement of the surrounding rock at drilling *F* is 103.47 mm, with 86.01% of the deformation occurring within a 5 m radius of the surrounding rock. This discrepancy can be attributed to drilling F's proximity to a significant deformation zone within the roadway. These findings shed light on the varying absolute displacements in the surrounding rock, offering insights into the deformation patterns associated with different drilling locations.

2.4. System Validation. To validate the accuracy of the earlier test results and data collection method, the "convergence gauge method" [50] was employed to monitor the displacement of the roadway surface in section 2 over the same period. The displacement of the roadway surface was measured every 7 days, and a total of thirteen measurements were taken. Given the challenges in monitoring the deformation of the surrounding rock at the roadway shoulder via surface displacement tracking, the analysis focused solely on the displacement of the right side and the roof of the

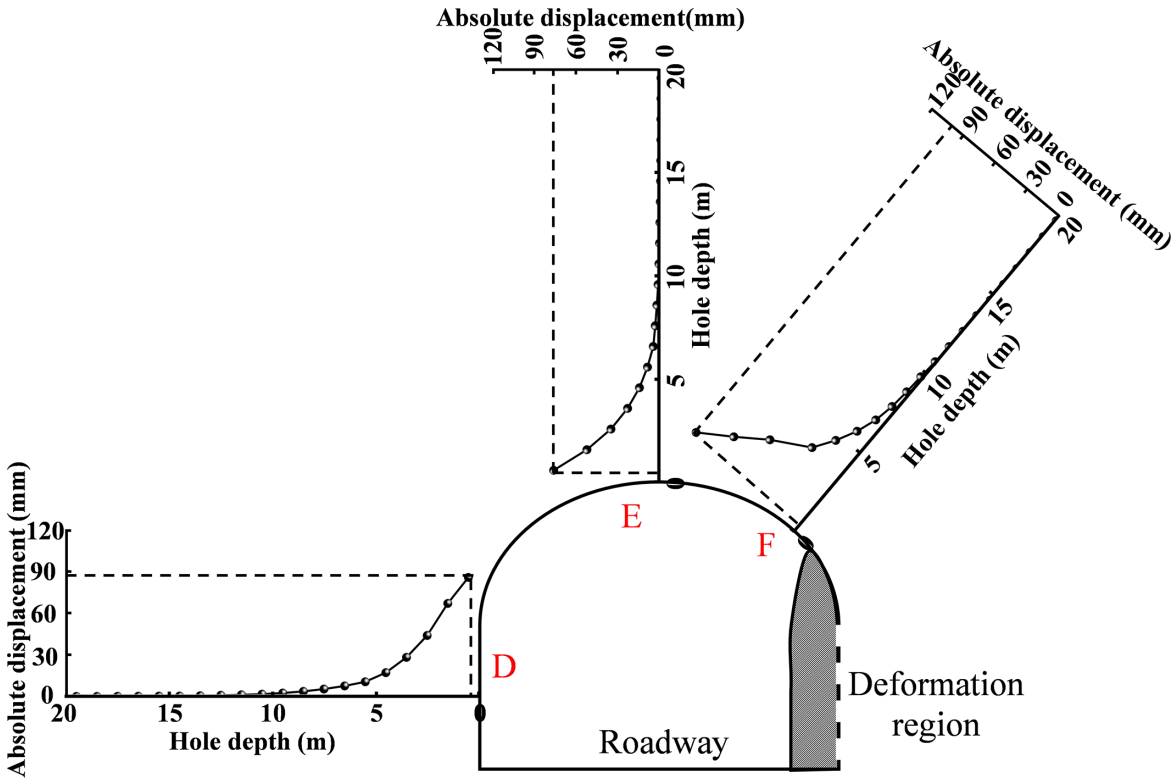

Figure 18: Monitoring section 2 roadway surrounding rock absolute displacement distribution map.

roadway. The results of the roadway surface displacement monitoring and RTDMS monitoring results are plotted as a roadway surface displacement curve on monitoring section 2 (Figure 19). The comparison test shows that the change rule of the roadway surface displacement monitoring results is consistent with the results obtained through the calculation of the deep surrounding rock. Consequently, it can be shown that the results of the deep deformation test for this system are accurate and effective.

The surface displacements of the roadway gang were 85.74 mm and 81.76 mm, while the surface displacements of the roadway top were 76.45 mm and 72.66 mm. In comparison, the RTDMS results were slightly higher, with corresponding errors of 4.64% and 4.96%. This is because the deformation direction of the deep surrounding rock is not entirely parallel to the vertical direction of the roadway surface. As a result, the surface displacement values obtained from deep displacement calculations are greater than the results of the roadway surface displacement monitoring. Furthermore, measurement errors during the monitoring process and variations in the monitoring environment also influenced the discrepancies in the monitoring results.

2.5. Engineering Practices. Although the monitoring section 1 is located at the junction of the roadway and the fault, the overall support structure integrity of this roadway has been maintained. An analysis of the strain data from the surrounding rock in the vicinity of the roadway reveals that the strain values at various locations along the roadway are all below 100 με. The deformation of the surrounding rock is primarily elastic, indicating that the roadway is in a stable state overall. The surrounding rock on the surface of the roadway has not changed significantly, and the structure of the surrounding rock is intact. Therefore, there is no need to repair the surrounding rock of the roadway, and the conditions for the passage of the rail transport roadway are good.

Traditional monitoring of the surrounding rock structure is primarily based on identifying the boundary of the rupture zone by observing sudden changes in the properties of the surrounding rock [51]. In essence, it is the search for the boundary between shallow discrete rock bodies and deep continuous rock bodies under the influence of stress redistribution. This approach can similarly be employed to monitor changes in the deformation of the surrounding rock by using the point of strain mutation as the boundary marker of the rupture zone. Therefore, data collected over 90 days have been analyzed, leading to the development of a final curve illustrating the rate of strain change at different depths within the surrounding rock (Figure 20).

As depicted in Figure 20, the strain points of drillings D and E are located at 1–2 m of surrounding rock, while the strain points of drilling *F* are located at 2–3 m of surrounding rock. It can be observed from the curves that the rate of strain change in the shallow surrounding rock varies significantly and irregularly. This variation is caused by the overturning and misalignment of the discrete rock bodies following the rupture of the shallow surrounding rock. Among them, a negative strain rate is present in the shallow surrounding rock at drillings D and F. This is because the monitoring of the rupture zone is initiated

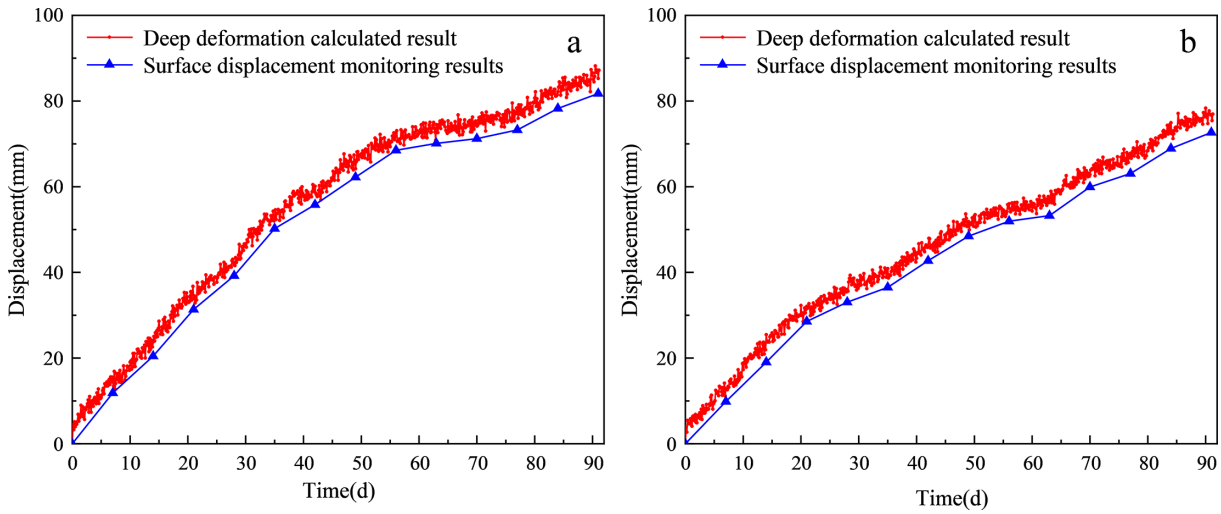

Figure 19: Monitoring section 2 roadway surrounding rock absolute displacement distribution map. (a) Left side. (b) Roof.

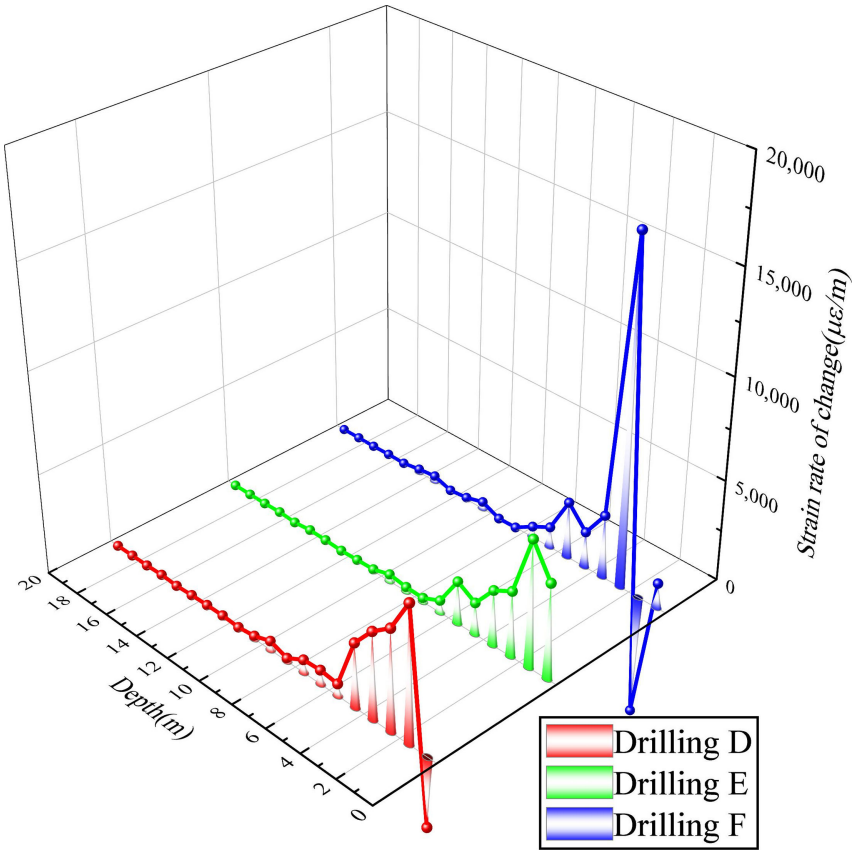

Figure 20: Strain change rate curve of monitoring section 2.

after it has undergone a certain period of development. The fractured and expanded perimeter rock at the boundary of the rupture zone squeezes the shallow fractured rock, which reduces the expansion rate of the shallow perimeter rock to a certain extent.

It can be observed that the boundary of the rupture zone between the left side and the top of the surrounding rock is approximately 2 m, whereas the boundary of the rupture zone of the right shoulder is around 3 m. Within this range, the integrity of the surrounding rock has been compromised, and the rock body exhibits a fragmented state. The strain rate of the surrounding rock within 6 m of each drilling is still significant, while the strain rate of the surrounding rock beyond 6 m tends to approach zero. Therefore, this boundary is considered as the limit of the damage zone in the surrounding rock. The surrounding rock in this zone is obviously subject to stress redistribution. The integrity of the surrounding rock has not yet been

damaged and is in a state of transition from discrete to continuous. Therefore, compared with the deep elastic zone, the surrounding rock exhibits a noticeable change in strain rate, whereas compared with the rupture zone, the surrounding rock displays a continuous pattern of change.

In Guqiao Mine, the supporting organizations in the monitoring section 2 of the belt conveyor roadway failed to control the deformation of the surrounding rock, resulting in a noticeable displacement of the right gang position of the roadway. Surrounding rock deformation monitoring results show that the surrounding rock is still undergoing continuous deformation, and the overall condition of the surrounding rock is unstable. Upon analyzing the results of surrounding rock deformation, it is evident that the top of the roadway and the left gang surrounding rock rupture zone have developed up to 2 m, while the right shoulder surrounding rock rupture zone has developed up to 3 m. Additionally, the surrounding rock within a 6 m radius has accumulated stresses. At the same time, the surrounding rock within a 6 m radius is clearly affected by stress redistribution and is within the damage zone.

Thus, some suggestions are made for the subsequent repair work of the roadway: (1) Due to the rupture of the shallow surrounding rock, it is recommended to grout and reinforce the surrounding rock within 3 m in order to restore its mechanical properties. (2) Due to the varying degrees of damage to the surrounding rock within a 6 m range, the roadway should be reinforced with anchor cables that are at least 7 m long. This will enhance the bearing capacity of the shallow surrounding rock. This is done to transfer the stress from the shallow surrounding rock to the deep, intact surrounding rock using high-strength anchor cables. This allows the surrounding rock to fully utilize its bearing capacity. (3) The roadway at the site has experienced significant deformation, and the surrounding rock has shown no signs of convergence, indicating that it is continuously deforming. In order to prevent the expansion of the surrounding rock rupture zone and the increased difficulty of support in the damaged zone, it is necessary to promptly carry out repairs and reinforcement support on the roadway.

3. Discussion

Currently, the significant deformation of the surrounding rock in deep roadways has become a primary constraint on the exploitation of deep resources. The real-time and precise monitoring of surrounding rock deformation in deep roadways is of significant importance for the assessment of the stability status of the surrounding rock and the guidance of support interventions. However, existing surface displacement monitoring methods and multipoint displacement meters are inadequate for achieving real-time monitoring with large range and high precision. Meanwhile, ordinary FBG sensors are limited in the number of measurement points, and they are difficult to use for precise monitoring due to spatial resolution constraints. Distributed FBG sensors have lower measurement accuracy, and the cost of demodulation equipment is high, making them challenging to apply on a large scale in the field (Table 3).

This article presents a large-range quasi-distributed strain-sensing optical fiber based on the IWFBG technology. It enables the submeter placement and micrometer-level monitoring of surrounding rock structures. Numerous indoor experiments have demonstrated that the strain values during rock fracture range from 0.8% to 1.4% [52]. Due to the limitations of commercially available demodulation equipment with a central wavelength range of 1528–1568 nm, the designed measurement range for SSC strain is 0%–3%. When the rock strain exceeds 3% but has not reached the maximum strain value of the fiber core (5%), SSC can still monitor the deformation of deep surrounding rock. For field applications, it is possible to use bidirectional excitation, enabling monitoring of deep surrounding rock deformation even after superficial fiber fractures. To expand the measurement range, the system can be enhanced by introducing demodulation devices with a broader demodulation range, building upon the existing RTDMS. In future research, increasing the monitoring range can be achieved by enhancing the density of shallow surrounding rock measurement points.

This article is based on a 90-day on-site test of the RTDMS at the Guqiao Coal Mine, utilizing two roadway sections. Deformation monitoring data for both stable and less stable surrounding rock were obtained. The stability and accuracy of the RTDMS were confirmed by comparing the results with surface displacement monitoring of the roadway. In the subsequent research, further cross-comparisons with other measurement methods will be carried out to gather additional data for verification and feedback analysis.

By processing the acquired data on surrounding rock strain, it is possible to calculate the strain variation rates at different depths of the surrounding rock, allowing for the determination of the distribution of rupture zones in the rock. These data provide essential support for assessing the stability of the surrounding rock and planning subsequent roadway maintenance and support work. Furthermore, by combining this system with surrounding rock stress monitoring sensors, comprehensive monitoring of stress fields and deformation fields during the evolution of surrounding rock fracture in deep roadways can be achieved, offering on-site data support for further understanding the significant deformation and instability of deep roadway surrounding rock. As this technology is increasingly applied in tunnels with varying geological conditions, rock types, and cross-sectional shapes, the wealth of field monitoring data obtained can be utilized to construct a comprehensive model for the evolution of instability in deep tunnel surrounding rock. This, in turn, enables the implementation of intelligent decision-making for support intervention processes.

4. Conclusion

In response to the monitoring challenges related to the deformation of deep roadway surrounding rock, a high-range quasi-distributed strain sensing optical fiber cable has

Table 3: Roadway deformation monitoring method.

Comparative content		Multipoint displacement meter	Ordinary FBG sensors	Distributed FBG sensors	IWFBG sensors
Measuring range (με)		0–20,000	±15,000	±15,000	0–50,000
Number of measuring points		≤5 points	≤10 points	>3000 points	>3000 points
Measuring accuracy (με)		±20	±20	±100	±20
Spatial resolution (m)		2–4	7–10	0.2	0.5
Cost ($)	Sensors	2500	1500	2500	2500
	Demodulator	7000–13,000	13,000	>82,000	<35,000

been developed. The performance of this SSC was tested through laboratory calibration. Furthermore, a demodulator and monitoring software were developed based on SSC, leading to the establishment of RTDMS, which was subsequently applied in field engineering. The main conclusions are as follows:

(1) SSC was developed using a high-strain optical fiber core based on IWFBG technology, capable of withstanding up to 5% strain. The spatial resolution of the SSC is 1 m, and the strain range is 0%–3%. The strain sensitivity coefficient of SSC is 1.23 pm/με, and the temperature sensitivity coefficient is 10.78 pm/°C obtained through indoor calibration testing. The accuracy levels are all within 0.5, demonstrating excellent linearity and testing accuracy.

(2) RTDMS consists of SSCs, strain demodulator, associated installation equipment, and monitoring software. Following the principles of SSC monitoring, the on-site testing procedures were standardized. This system enables the submeter arrangement of measuring points on the deep tunnel surrounding rock structure and achieves micrometer-level monitoring of surrounding rock deformation. The flexible networking approach has facilitated real-time remote monitoring of surrounding rock deformation in various engineering scenarios.

(3) The engineering application of RTDMS was carried out by relying on the rail transport roadway (II) and belt conveyor roadway of Guqiao Mine. The maximum strain value of the monitoring result is 27,095 με, and the maximum displacement of the roadway surface is 103.47 mm. At the same time, the system was validated by comparing the surface displacement of the roadway. The errors in the test results were found to be 4.64% and 4.96%. These results indicate that the deep deformation test results of the roadway obtained from this system are accurate and valid. After analysis, the deepest point of the rock rupture zone within the perimeter is 3 m, and the boundary of the rock damage zone extends up to 6 m. The monitoring results provide valuable insights and recommendations for the excavation, repair, and structural support of the roadways.

Data Availability

The datasets used and/or analyzed during the current study are available from the corresponding author on reasonable request.

Conflicts of Interest

The author(s) declare(s) that there is no conflict of interest regarding the publication of this paper.

Acknowledgments

This work was supported by the National Natural Science Foundation of China (Grant No. 51874275).

References

[1] H. P. Xie, "Research framework and anticipated results of deep rock mechanics and mining theory," *Advanced Engineering Sciences*, vol. 49, no. 2, pp. 1–16, 2017.

[2] H. P. Kang, G. F. Wang, P. F. Jiang, J. C. Wang, and N. Zhang, "Conception for Strata control and intelligent mining technology in deep coal mines with depth more than 1000 m," *Journal of China Coal Society*, vol. 43, no. 7, pp. 1789–1800, 2018.

[3] H. P. Kang, "Seventy years development and prospects of Strata control Technologies for coal mine roadways in China," *Chinese Journal of Rock Mechanics and Engineering*, vol. 40, no. 1, pp. 1–30, 2021.

[4] B. T. Shen, "Coal mine roadway stability in soft rock: A case study," *Rock Mechanics and Rock Engineering*, vol. 47, no. 6, pp. 2225–2238, 2014.

[5] H. P. Kang, M. J. Fan, F. Q. Gao, and H. Zhang, "Deformation and support of rock roadway at depth more than 1 000 meters," *Chinese Journal of Rock Mechanics and Engineering*, vol. 34, no. 11, pp. 2227–2241, 2015.

[6] S. Q. Yang, M. Chen, H. W. Jing, K. F. Chen, and B. Meng, "A case study on large deformation failure mechanism of deep soft rock roadway in Xin'An coal mine," *Engineering Geology*, vol. 217, pp. 89–101, 2017.

[7] H. W. Jing, Q. B. Meng, J. F. Zhu, B. Meng, and L. Y. Wei, "Theoretical and technical progress of stability control of

broken rock zone of deep roadway surrounding rock," *Journal of Mining and Safety Engineering*, vol. 37, no. 3, pp. 429–442, 2020.

[8] H. Jing and Y. Li, "Application of Minetcs in the deformation monitoring of roadway," *Arabian Journal for Science and Engineering*, vol. 44, no. 5, pp. 4587–4595, 2019.

[9] J. Wang, J. G. Ning, Y. L. Tan, S. C. Hu, and W. Y. Guo, "Deformation and failure laws of roadway surrounding rock and support optimization during shallow-buried multi-seam mining," *Geomatics, Natural Hazards and Risk*, vol. 11, no. 1, pp. 191–211, 2020.

[10] Z. J. Wang, D. Xie, J. Y. Fan, Y. T. Mao, and Z. G. Tao, "Study on deformation mechanism and large deformation control method of a strongly weathered Carbonaceous slate tunnel in Western China," *Journal of Geomechanics*, 1–16, 2023.

[11] J. Guo, J. S. Yang, W. Chen, D. Shen, and T. Liu, "Research on large deformation of surrounding rock and mechanical characteristics of lining of Carbonaceous slate tunnel based on field measurement," *Chinese Journal of Rock Mechanics and Engineering*, vol. 38, no. 4, pp. 832–841, 2019.

[12] J. K. Xu, E. Y. Wang, and R. Zhou, "Real-time measuring and warning of surrounding rock dynamic deformation and failure in deep roadway based on machine vision method," *Measurement*, vol. 149, p. 107028, 2020.

[13] P. Shan, C. Yan, X. Lai, H. Sun, C. Li, and X. Chen, "Evaluation of real-time perception of deformation state of host rocks in coal mine roadways in dusty environment," *Sustainability*, vol. 15, no. 3, p. 2816, 2023.

[14] Y.-M. Zhao, X.-T. Feng, Q. Jiang, et al., "Large deformation control of deep roadways in fractured hard rock based on cracking-restraint method," *Rock Mechanics and Rock Engineering*, vol. 54, no. 5, pp. 2559–2580, 2021.

[15] Z. Xie, N. Zhang, X. Feng, D. Liang, Q. Wei, and M. Weng, "Investigation on the evolution and control of surrounding rock fracture under different supporting conditions in deep roadway during excavation period," *International Journal of Rock Mechanics and Mining Sciences*, vol. 123, p. 104122, 2019.

[16] X. Tan, W. Chen, H. Liu, et al., "A combined supporting system based on foamed concrete and U-shaped steel for underground coal mine roadways undergoing large Deformations," *Tunnelling and Underground Space Technology*, vol. 68, pp. 196–210, 2017.

[17] J. Cui, W. Wang, Q. Jia, G. Peng, H. Wu, and P. Wang, "Measurement and analysis of roadway deformation and stress under mining-induced stress," *Shock and Vibration*, vol. 2021, pp. 1–9, 2021.

[18] B. Shen, A. King, and H. Guo, "Displacement, stress and Seismicity in roadway roofs during mining-induced failure," *International Journal of Rock Mechanics and Mining Sciences*, vol. 45, no. 5, pp. 672–688, 2008.

[19] Y. G. Yang and N. Fan, "Experimental study on surrounding rock loosing circle by single-hole acoustic wave testing method," *Coal Science and Technology*, vol. 47, no. 3, pp. 93–100, 2019.

[20] V. Kumar, V. Kumar, E. Kalyan Kumar, A. Gangwar, and S. K. Panda, "Acoustic emission-based structural health prediction and monitoring: A comprehensive review," *International Journal of Applied Mechanics*, vol. 15, no. 9, pp. 12–34, 2023.

[21] X. X. Yang, W. Q. Wang, and H. W. Jing, "Analysis and comparison on conventional loose zone measuring and test methods," Coal Science and Technology, vol. 40, no.08, pp. 1-5+54, 2012.

[22] L. Guo, J. C. Li, Z. C. Zhang, and S. J. Cheng, "Research on surrounding rock loose zone of tunnel under unsymmetrical loading with ground penetrating radar and its application," Chinese Journal of Rock Mechanics and Engineering, vol. 30, no.S1, pp. 3009-3015, 2011.

[23] Y. H. Liu, "The fiber grating sensors technology and its applications," SensorWorld, vol. 3, pp. 20-23, 2005.

[24] C. Caucheteur, K. Chah, F. Lhomme, M. Blondel, and P. Megret. "Autocorrelation demodulation technique for fiber Bragg grating sensor," IEEE Photonics Technology Letters, vol. 16, no.10, pp. 2320-2322, 2004.

[25] G. Q. Xv, and D. Y. Xiong, "Applications of fiber Bragg grating sensing technology in engineering," Chinese Optics, vol. 6, no.03, pp. 306-317, 2013.

[26] C. Y. Hong, Q. Yang, Y. Zhao, D. W. Chen, and W. Yu, "Strain monitoring mechanism of geogrids based on optical fiber sensing technology," Rock and Soil Mechanics, vol. 42, no.06, pp. 1755-1764, 2021.

[27] A. Laudati, F. Mennella, M. Esposito, A. Cusano, and M. Giordano, "A fiber optic Bragg grating seismic sensor," Third European Workshop on Optical Fiber Sensors, vol. 6619, pp. 247-250, 2007.

[28] M. R. Islam, M. M. I. Khan, A. M. Al Naser, et al., "Design of a QUAD channel SPR-based PCF sensor for Analyte, strain, temperature, and magnetic field strength sensing, " *Optical and Quantum Electronics*, vol. 54, no. 9, 2022.

[29] Z. G. Zhao, Y. J. Zhang, C. Li, Z. Wan, and Y. N. Li, "Monitoring of coal mine roadway roof separation based on fiber Bragg grating displacement sensors," International Journal of Rock Mechanics and Mining Sciences, vol. 74, pp. 128-132, 2015.

[30] R. Z. You, L. Ren, and G. B. Song, "A novel fiber Bragg grating (FBG) soil strain sensor," Measurement, vol. 139, pp. 85-91, 2019.

[31] A. Motil, A. Bergman, and M. Tur, "[INVITED] state of the art of Brillouin fiber-optic distributed sensing, " *Optics & Laser Technology*, vol. 78, pp. 81–103, 2016.

[32] B. Tang and H. Cheng, "Application of distributed optical fiber sensing technology in surrounding rock deformation control of TBM-Excavated coal mine roadway," *Journal of Sensors*, vol. 2018, pp. 1–10, 2018.

[33] L. Tartara, C. Codemard, J. N. Maran, R. Cherif, and M. Zghal, "Full modal analysis of the Brillouin gain spectrum of an optical fiber," Optics Communications, vol. 282, no.12, pp. 2431-2436, 2009.

[34] X. Wang, B. Shi, G. Q. Wei, S. E. Chen, and H. H. Zhu, "Monitoring the behavior of segment joints in a shield tunnel using distributed fiber optic sensors," Structural Control and Health Monitoring, vol. 25 Article ID e2056, 2018.

[35] B. Y. Sun, P. S. Zhang, and M. R. Fu, "Comparative study on the "optic-electric" monitoring method for the deformation and failure of surrounding rock in stopes," Nat Hazards, vol. 110, pp. 407-27, 2022.

[36] M. L. Zhang, Q. Z. Sun, Z. Wang, X. L. Li, and H. R. Liu, "Investigation on distributed optical fiber sensor based on

identical-low-reflective fiber gratings," Laser & Optoelectronics Progress, vol. 48, no.08, pp. 93-98, 2011.

[37] B. Li, K. Li, and S. Jiang, "Research of practical demodulation system based on Ultra Weak FBG array," Electronic Design Engineering, vol. 31, no.7, pp. 146-150+155, 2023.

[38] Y. M. Wang, C. C Hu, Q. Liu, H. Y. Guo, and G. L. Yin, "High speed demodulation method of identical weak fiber Bragg gratings based on wavelength-sweep optical time-domain reflectometry." Acta Phys Sin, vol. 65, no.20, pp. 133-142, 2016.

[39] S. C. Tjin, J. Z. Hao, Y. Z. Lam, Y. C. Ho, and N. B. Koon, "A Pressure Sensor Using Fiber Bragg Grating," Fiber and Integrated Optics, vol. 20, no.1, 313-318, 2001.

[40] C. L. Li, J. G. Tang, Y. S. Jiang, C. Cheng, and L. B. Cai, "Distributed Vibration Detection System Based on Weak Fiber Bragg Grating Array" IEEE Photonics Journal, vol. 12, no.4, 2017.

[41] Z. H. Luo, H. Q. Wen, H. Y. Guo, and M. H. Yang, "A time- and wavelength-division multiplexing sensor network with ultra-weak fiber Bragg gratings," Opt Express, vol. 21, no.19, pp. 22799-22807, 2013.

[42] C. Wang, Y. Shang, X. H. Liu, C. Wang, and H. H. Yu, "Distributed OTDR-interferometric sensing network with identical ultra-weak fiber Bragg gratings," Opt Express, vol. 23, no.22, pp. 29038-29046, 2015.

[43] M. L. Zhang, Q. Z. Sun, Z. Wang, X. L. Li, and H. R. Liu. "A large capacity sensing network with identical weak fiber Bragg gratings multiplexing," Optics Communications, vol. 285, no.13, pp. 3082-3087, 2012.

[44] K. Kuroda, "Wavelength-division Multiplexed interrogation of Fbgs using a distributed-feedback laser array, " *IEEE Photonics Technology Letters*, vol. 34, no. 10, pp. 509–512, 2022.

[45] W. Liang, Y. Y. Huang, Y. Xu, R. K. Lee, and A. Yariv, "Highly sensitive fiber Bragg grating refractive index sensors," Applied Physics Letters, vol. 86, no.15, 2005.

[46] B. Q. Liao, Q. D. Zhao, D. J. Feng, Y. L. Huang, and J. Li, "Coupled-mode theory for optical fiber and its application to fiber bragg grating," Acta Optica Sinica, vol. 11, pp. 1340-1344, 2002.

[47] Z. Liang, D. Liu, X. Wang, et al., "FBG-based strain monitoring and temperature compensation for composite tank," *Aerospace Science and Technology*, vol. 127, p. 107724, 2022.

[48] J. Wu, S. Xu, L. Qi, Z. Meng, L. Jia, and C.-M. Chang, "Life cycle monitoring of offshore steel pipe piles via UWFBG Wireless sensor network," *Structural Control and Health Monitoring*, vol. 2023, pp. 1–18, 2023.

[49] Q. S. Liu, Y. S. Kang, and Y. Q. Bai. "Research on supporting method for deep rock roadway with broken and soft surrounding rock in Guqiao Coal Mine," Rock and Soil Mechanics, vol. 30, no.10, pp. 3097-3104, 2011.

[50] J. Wang, Z. J. Zhang, T. C. Zhu, M. C. He, and W. L. Gong, "Model test study on deformation mechanisms of roadways supported by constant resistance and large deformation anchor cables," Chinese Journal of Rock Mechanics and Engineering, vol. 39, no.09, pp. 927-937, 2020.

[51] H. Y. Zou, M. Xiao, "Study of methodology for assessment of excavation disturbed zone of underground caverns," Chinese Journal of Rock Mechanics and Engineering, vol. 29, no.03, pp. 513-519, 2010.

[52] Q. B. Zhang, and J. Zhao, "A review of dynamic experimental techniques and mechanical behaviour of rock materials," Rock Mech Rock Eng, vol. 47, pp. 1411–1478, 2014.